Regular Article

PHYSICAL CHEMISTRY RESEARCH
Published by the
Iranian Chemical Society
www.physchemres.org
info@physchemres.org

Phys. Chem. Res., Vol. 14, No. 1, 9-27, March 2026
DOI: 10.22036/pcr.2025.540201.2722

Synthesis, SC-XRD, HSA, DFT Calculations, and Molecular Docking Studies of a New Cu^{I} Complex Bearing the Bidentate Schiff Base Derived from Trimethylenediamine and 4-Cyanobenzaldehyde

H. Kargar[a,*], F. Abyar[a], M. Fallah-Mehrjardi[b,*], E. Acar[c], N. Dege[c], M. Ashfaq[d], K.S. Munawar[e,f] and M.N. Tahir[d]

[a]*Department of Chemical Engineering, Faculty of Engineering, Ardakan University, P.O. Box: 184, Ardakan, Iran*
[b]*Department of Chemistry, Payame Noor University (PNU), 19395-4697, Tehran, Iran*
[c]*Department of Physics, Faculty of Science, Ondokuz Mayıs University, 55200, Samsun, Turkey*
[d]*Department of Physics, University of Sargodha, Punjab, 40100, Pakistan*
[e]*Institute of Chemistry, University of Sargodha, Punjab, 40100, Pakistan*
[f]*Department of Chemistry, University of Mianwali, Mianwali, 42200, Pakistan*
(Received 9 August 2025, Accepted 7 November 2025)

We report the synthesis and characterization of a new tetranuclear Cu(I) complex, **$[Cu_2(L^{4CN})\mu_2\text{-}I]_2$**, derived from a Salpn-type Schiff base ligand (**L^{4CN}** = 4,4'-[propane-1,3-diylbis(nitrilomethylidyne)]dibenzonitrile). Single-crystal XRD revealed a structure where each copper center adopts a distorted trigonal planar geometry, coordinated by two iodide ligands and one imine N-atom. N-atoms of cyano groups facilitate intermolecular interactions, stabilizing the solid-state assembly, as confirmed by Hirshfeld surface analysis. Computational studies (FMO, MEP, NBO, NPA) probed the electronic structure. NPA indicated positive charges on copper centers and negative charges on donor atoms, highlighting charge transfer. Ligand orbitals were found to significantly support the metal centers, with electron density variations reflecting the complex architecture. Second-order perturbation analysis explained electron flow and stabilization pathways. Molecular docking revealed stable binding sites with DNA and strong interactions with BSA at active sites, indicating possible biochemical relevance. These results highlight the biochemical effects of these metal complexes.

Keywords: Copper(I) complex, Schiff base, SC-XRD, Density Functional Theory, Molecular docking

INTRODUCTION

Schiff base ligands represent a prominent class of ligands widely recognized for their structural flexibility, ease of formation, and ability to incorporate various donor groups [1-3]. They are typically synthesized through the condensation of primary amines with aromatic/aliphatic aldehydes or ketones and are characterized by the presence of a carbon to nitrogen double bond (HC=N) [4]. Among these, the NN donor ligands contain two nitrogen atoms, each capable of donating a lone pair of electrons. This allows the ligand to coordinate to a metal ion at two distinct donor sites, forming a stable chelate ring and enhancing the overall stability of the resulting metal complex [5]. To synthesize a bidentate NN-donor Schiff base ligand, a diamine is typically reacted with a carbonyl compound containing at least one aldehyde or ketone functional group [6].

Schiff bases form stable coordination complexes with a wide range of transition metal ions due to their strong chelating ability. These complexes have found applications in diverse fields, including photochromism, hydrometallurgy, and dye manufacturing [7-9]. Moreover, Schiff base metal complexes have demonstrated promising

*Corresponding authors. E-mail: h.kargar@ardakan.ac.ir; fallah.mehrjerdi@pnu.ac.ir

biological activities, particularly in antimicrobial and anticancer research [10]. In addition, these complexes have been utilized in the development of gas storage materials and have found significant applications in catalysis [11].

The distinctive photophysical characteristics of coinage metal complexes with a d^{10} electronic configuration, which are based on structural adaptability, have garnered more and more attention [12,13]. The absence of d–d excited states in these complexes is advantageous, as it eliminates nonradiative deactivation pathways from the excited to the ground state [14]. Among them, copper(I) coordination chemistry has gained a lot of attention because of the metal's versatile coordination geometries, closed-shell electronic configuration, and applications in materials science, bioinorganic chemistry, and catalysis [15-17]. Over the last few years, a great deal of study has been done in this field due to the structural variety of coordination polymers based on copper iodide [18-20]. The ability of Schiff bases to stabilize both Cu(I) and Cu(II) oxidation states makes them excellent ligands for coordination chemistry [21].

Theoretical investigations, such as DFT and TD-DFT, have been a useful tool in the investigation of electronic structures, reactivity parameters, and spectroscopic characteristics of Cu(I) Schiff base complexes. The design of functional Cu(I)-based materials is guided by these theoretical techniques, which also help to comprehend structure–property correlations [22,23].

Herein, we are reporting the synthesis, crystal structure, and spectroscopic and theoretical investigation of a novel Cu(I) Schiff base complex in continuation of our earlier findings [24,25]. This work primarily focuses on their supramolecular assembly, photophysical properties, and potential significance in the development of functional materials.

EXPERIMENTAL

Materials and Methods

The solvents and chemicals employed in this study were of analytical grade and procured from Sigma-Aldrich. Elemental analysis (CHN) for the ligand and its copper complex was performed using a Heraeus CHN-O-FLASH EA 1112 analyzer. Infrared spectra were obtained on a Shimadzu IR Prestige-21 spectrophotometer to assess vibrational modes. ^{1}H and ^{13}C NMR spectra were acquired on a Bruker AVANCE 500 MHz instrument, with chemical shifts referenced to tetramethylsilane (TMS) in parts per million (ppm).

Single Crystal Procedure from Selection to Refinement

An optical microscope was used for crystal selection, followed by data collection using a STOE IPDS 2 diffractometer. Absorption correction was done by the integration method, and STOE X-RED [26] software was used for this. The structure was initially solved using SHELXT 2014 [27] and subsequently refined using SHELXL 2019/2 [28]. Hydrogen atoms were placed using the riding model, and their isotropic displacement parameters were fixed accordingly. ORTEP-III [29] and mercury [30] software were used to display results.

Synthesis of Schiff Base Ligand and its Copper(I) Complex

A solution of 4-cyanobenzaldehyde (2 mmol, 0.262 g) was prepared in 30 m; of chloroform. In a separate vial, trimethylenediamine (1 mmol, 0.074 g) was dissolved in 5 ml of chloroform. The diamine solution was slowly added to the aldehyde solution and stirred at room temperature for 3 h. The precipitated product was collected by filtration, washed with chilled methanol, and recrystallized from hot ethanol to yield colorless crystals of the Schiff base ligand.

Yield = 81%, Anal. Calcd. (Found) for $C_{19}H_{16}N_4$: C, 75.98 (76.22); H, 5.37 (5.46); N, 18.65 (18.53)%. FT-IR (KBr, cm^{-1}): ν = 3057 (=CH), 2901 (–CH_2), 2845 (–CH=N), 2224 (–C≡N–), 1641 (–C=N–), 1454–1562 (–C=C–). ^{1}H NMR (500 MHz, $CDCl_3$, ppm): δ = 8.39 [s, 2H, HC=N], 7.87 [d, ^{3}J = 8.2 Hz, 2H, aromatic], 7.74 [d, ^{3}J = 8.2 Hz, 2H, aromatic], 3.82 [t, ^{3}J = 6.8 Hz, 4H, CH_2–N], 2.17 [quin., ^{3}J = 6.8 Hz, 2H, CH_2].

The Cu(I) complex was prepared by dissolving the Schiff base ligand (0.600 g, 2 mmol) in 30 ml of chloroform and adding it to a stirred THF solution (20 ml) containing CuI (0.380 g, 2 mmol). After stirring for 30 min, the solvent was partially removed under reduced pressure, reducing the volume to about 10 ml. Yellow crystals suitable for SC-XRD analysis were obtained by slow diffusion of diethyl ether vapor into the concentrated solution at room temperature (298 K).

Yield = 66%, Anal. Calcd. (Found) for $C_{19}H_{16}Cu_2I_2N_4$: C, 33.50 (33.69); H, 2.37 (2.42); N, 8.22 (8.03)%. FT-IR (KBr, cm^{-1}): ν = 3071 (=CH), 2922 ($-CH_2$), 2855 (–CH=N), 2226 (–C≡N–), 1626 (–C=N–), 1454–1564 (–C=C–). ^{1}H NMR (500 MHz, DMSO-d_6, ppm): δ = 8.49 [s, 2H,df HC=N], 7.99 [d, ^3J = 8.0 Hz, 2H, aromatic], 7.92 [d, ^3J = 8.0 Hz, 2H, aromatic], 3.77 [t, ^3J = 6.4 Hz, 4H, CH_2–N], 2.04 [quin., ^3J = 6.4 Hz, 2H, CH_2].

RESULTS AND DISCUSSION

Synthesis and Characterization

The *N,N*-bidentate Schiff base ligand was synthesized by reacting 4-cyanobenzaldehyde with trimethylenediamine in a 2:1 ratio. Upon the addition of CuI, the corresponding Cu(I) complex was formed as a dimer (Scheme 1).

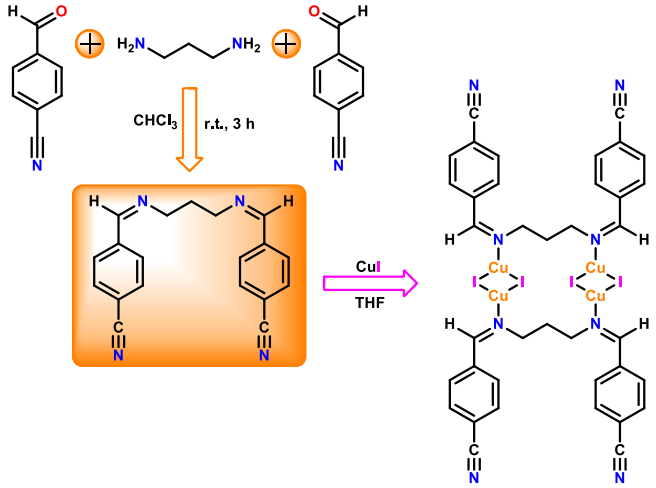

Scheme 1. Synthesis route of bidentate Schiff base ligand and its copper(I) complex

The structures of both the ligand and the complex were confirmed by FT-IR and ^{1}H NMR spectroscopy. Their spectra were quite similar, indicating that the ligand's structure remained largely unchanged upon complexation, with only the two imine nitrogen atoms coordinating to the metal ions. In the FT-IR spectrum of the free ligand, characteristic vibrational bands appeared at 1641 cm^{-1} (azomethine, C=N) and 2224 cm^{-1} (cyano, C≡N). Upon complexation, the azomethine band shifted to a lower wavenumber (1626 cm^{-1}), indicating a reduction in C=N bond order due to coordination with Cu(I). In contrast, the cyano stretching vibration remained nearly unchanged (2226 cm^{-1}), confirming its non-involvement in metal binding (Fig. 1).

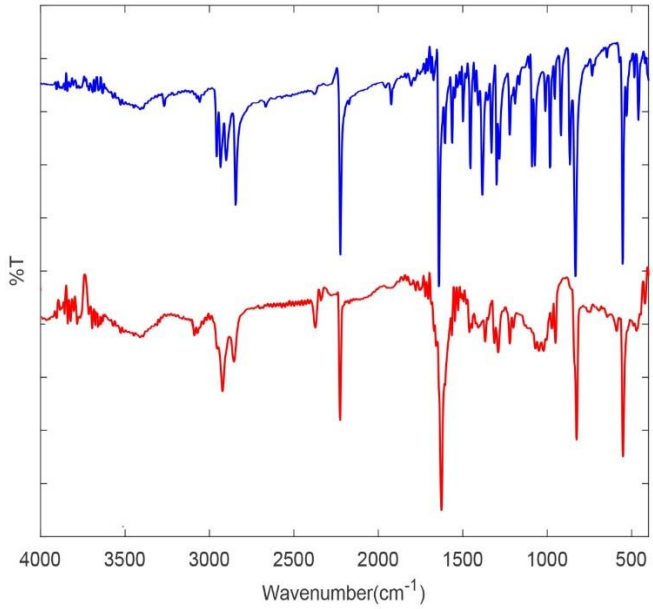

Fig. 1. FT-IR spectra of Schiff base ligand (blue) and its copper(I) complex (red).

The ^{1}H NMR spectra of both the ligand and its complex exhibited symmetrical patterns (Figs. 2 and 3). In the ligand´s spectrum, the methylene protons appeared as two distinct sets: a quintet signal at 2.17 ppm for the central methylene group and a triplet signal at 3.82 ppm for the remaining methylene protons. Similarly, in the complex spectrum, these protons were observed at 2.04 ppm (quintet) and 3.77 ppm (triplet), respectively. The aromatic protons appeared as two doublets at 7.74 ppm and 7.87 ppm in the spectrum of the ligand, shifting to 7.92 ppm and 7.99 ppm in the complex. Notably, the most prominent signal in both spectra appeared at 8.39 ppm for the ligand and 8.49 ppm for the complex, corresponding to the azomethine proton. The downfield shift observed in the complex indicates deshielding, which can be attributed to reduced electron density around the azomethine proton upon coordination with Cu(I) ions.

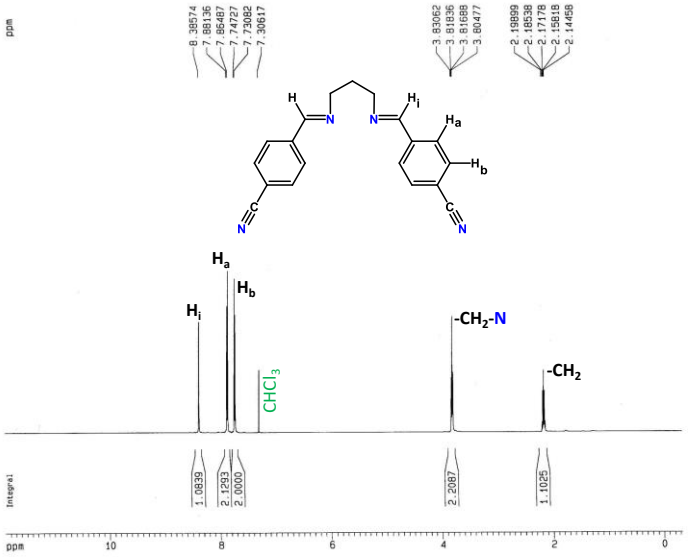

Fig. 2. ^{1}H NMR spectrum of Schiff base ligand in $CDCl_3$.

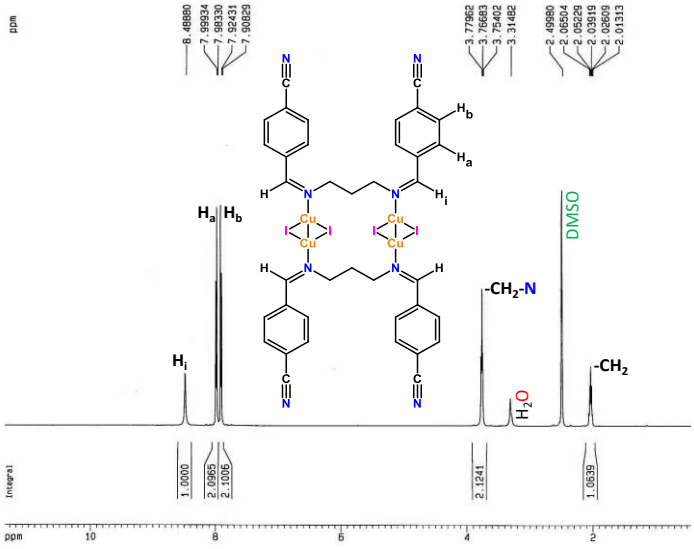

Fig. 3. ^{1}H NMR spectrum of copper(I) complex in DMSO-d_6.

Crystal Structure of $[Cu_2(L^{4CN})\mu_2\text{-}I]_2$

The molecular structure is a tetranuclear copper Schiff base complex, in which each copper atom is coordinated by two iodide ligands and one imine nitrogen atom (Fig. 4, Table 1). Within the coordination sphere, the geometry around each copper center is best described as distorted trigonal planar, as indicated by the variation in bond angles.

Table 1. Prominent SC-XRD Details

Chemical formula	$C_{19}H_{16}Cu_2I_2N_4$
M_r	681.26
Crystal system, space group	Monoclinic, $P2_1/m$
Temperature (K)	293
a, b, c (Å)	8.6815 (8), 33.193 (3), 8.7842 (8)
β (°)	119.572 (7)
V (Å^3)	2201.6 (4)
Z	4
Radiation type	Mo $K\alpha$
μ (mm^{-1})	4.75
Crystal size (mm)	0.40 × 0.30 × 0.22
Diffractometer	STOE *IPDS* 2
Absorption correction	Integration (*X-RED32*; Stoe & Cie, 2002)
No. of measured, independent and observed [$I > 2\sigma(I)$] reflections	10486, 2894, 1905
R_{int}	0.107
$(\sin\theta/\lambda)_{max}$ (Å^{-1})	0.537
$R[F^2 > 2\sigma(F^2)]$, $wR(F^2)$, S	0.158, 0.460, 1.79
No. of reflections	2894
No. of parameters	247
H-atom treatment	H-atom parameters constrained
$\Delta\rho_{max}$, $\Delta\rho_{min}$ (e Å^{-3})	7.02, -2.41

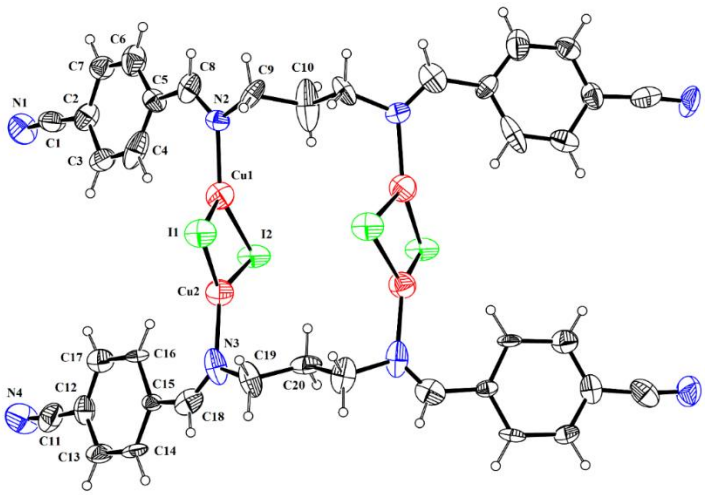

Fig. 4. Molecular structure at 30% atomic probability level.

For the Cu1 atom, the bond angles range from 109.8(5)° to 130.1(5)°, while for the Cu2 atom, they range from 109.3(6)° to 128.9(6)° (Table 2). The central part of the molecule (Cu1/Cu2/I1/I2) adopts a non-planar conformation with a puckering amplitude of 0.206(4) Å. It is inclined at 63.6(2)° and 63.5(2)° relative to the first (C1–C7/N1) and second (C11–C17/N4) cyano-substituted phenyl rings, respectively. The molecules are interlinked end to end by C–H···N bonding in the form of dimers, and as a result, $R_2^2(10)$ loops are formed (Fig. 5). The dimers are further connected by the same type of H-bonding. C(19) and C(9) molecular chains are formed *via* H-bonding, and these chains extend along the *b* and *c*-axis, respectively. Molecular aggregation is further stabilized due to π···π and C–N···π interactions with a centroid···centroid distance of 4.35 Å and N···π distance of 3.95 Å (Fig. 6, Table 3). The phenyl rings involved in π···π interactions are parallel to each other, with a dihedral angle between interacting rings is just 1°, but the rings are not exactly on one of each other, as the slippage or ring offset value is 2.344 Å. As per the Cambridge structural database, the geometrical parameters of **[Cu$_2$(L^{4CN})μ$_2$-I]$_2$** are consistent with literature structures with reference codes ANEFIJ (binuclear copper iodide complex) [31], JOJLUS (binuclear copper-cadmium iodide complex) [32], and VERGUU (binuclear copper iodide complex) [33].

Table 2. Important Geometrical Parameters Obtained from SC-XRD and DFT

Bond length (Å)	SC-XRD	DFT	Bond angle (°)	SC-XRD	DFT
I1–Cu2	2.553 (4)	2.64	Cu2–I1–Cu1	58.91 (12)	59.75
I1–Cu1	2.581 (4)	2.64	Cu2–I2–Cu1	59.58 (12)	60.51
I2–Cu2	2.529 (4)	2.61	N2–Cu1–I2	130.2 (5)	129.03
I2–Cu1	2.552 (4)	2.61	N2–Cu1–I1	109.8 (5)	111.49
Cu1–N2	1.945 (17)	2.03	I2–Cu1–I1	118.92 (16)	119.26
Cu2–N3	2.010 (3)	2.03	N3–Cu2–I2	128.8 (6)	128.92
			N3–Cu2–I1	109.3 (6)	111.59
			I2–Cu2–I1	120.85 (15)	119.28

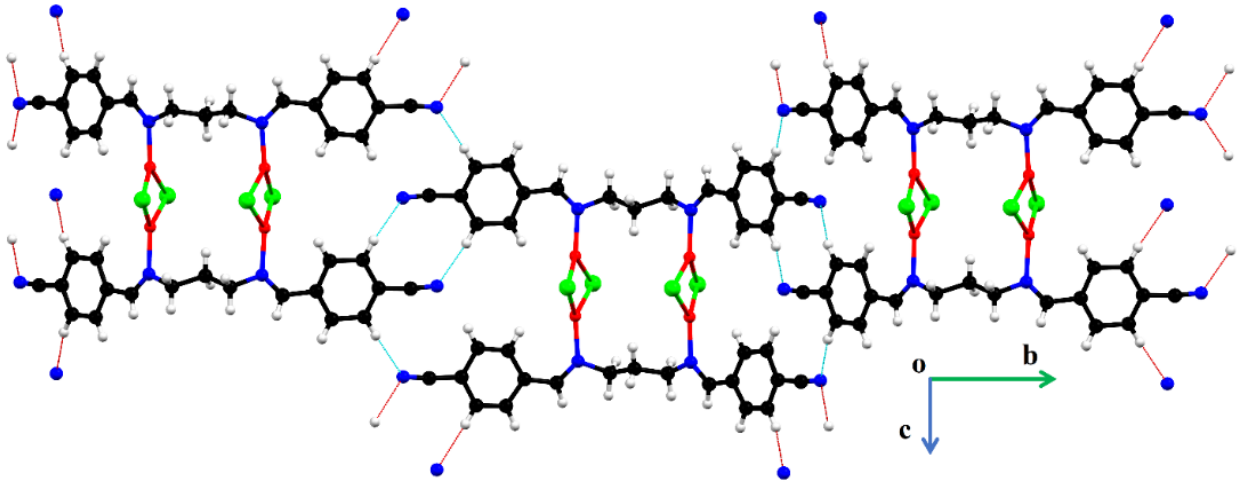

Fig. 5. The partial packing diagram illustrates the intermolecular connections formed through hydrogen bonding. Hydrogen bonds and weak (hanging) contacts are represented in sky blue and red, respectively.

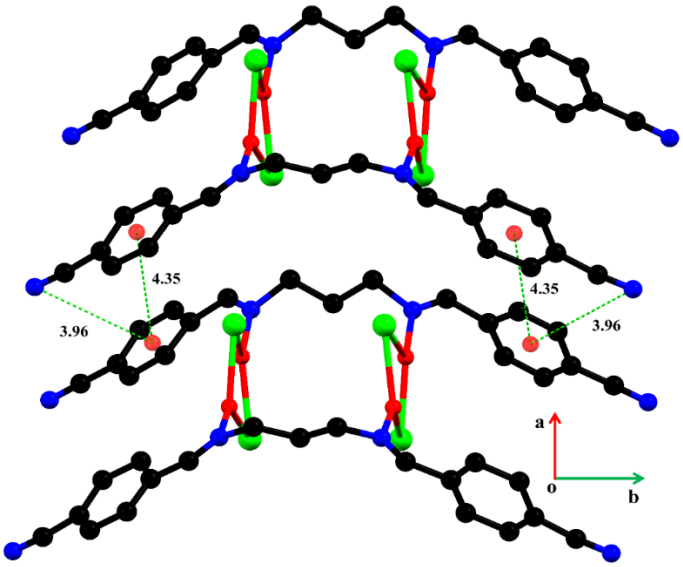

Fig. 6. Graphical representation of π···π and C–N···π interactions.

Table 3. Hydrogen-bond Geometry (Å, º) Along with C–N···π Interaction

D—H···*A*	*D*–H	H···*A*	*D*···*A*	<(*D*–H···*A*)°
C13–H13···N1^{i}	0.93	2.64	3.49	154
C17–H17···N4^{ii}	0.93	2.68	3.49	147
C—N···*π*	*C*–N	N···*π*	*C*···*π*	<(*C*–N···*π*)°
C11–N4···Cg1^{iii}	-	3.96	3.63	65 (2)

Symmetry codes: (i) −*x*, −*y*+1, −*z*; (ii) −*x*+1, −*y*+1, −*z*+2; (iii) *x*, *y*+1, *z*+1. Cg(1) is the centroid of the phenyl ring (C2–C7).

Hirshfeld Surface Analysis

Crystal Explorer v. 21.5 [34] offers a cost-effective and time-saving approach for visualizing and quantifying intermolecular interactions, thereby accelerating the understanding of crystal packing and stability. Hirshfeld surface, designed by considering normalized distances, identifies shorter and longer contacts and uses red, white, and blue patches to display shorter, equal, and longer contacts, respectively [35,36]. Figure 7a is the surface designed over normalized distances for **[Cu$_2$(L^{4CN})μ$_2$-I]$_2$**, on which red spots around cyano N-atoms and specific CH of phenyl rings indicate that these atoms formed short contacts. Moreover, the regions of particular shape enclosed in dashed ellipsoids on the shape index surface conformed existence of ring-involving interactions in **[Cu$_2$(L^{4CN})μ$_2$-I]$_2$** (Fig. 7b).

Interaction fragmentation analysis allows the contribution of each interatomic contact to solid-state aggregation to be determined [37,38], which is visualized through 2D fingerprint plots. Among these, the H···N contact is the major contributor to crystal packing, as the cyano nitrogen atoms participate in hydrogen-bonding interactions with $d_i \approx d_e \approx 1.1$ (Fig. 8a). Red and blue patches on the surface of Fig. 8d represent H···N contacts. The next top contributors are H···H, H···C, and C···C contacts. Enrichment ratio showed that carbon-carbon pair has the highest tendency to make crystal packing interactions, followed by hydrogen-nitrogen, hydrogen-iodine, and iodine-iodine pairs (Table 4).

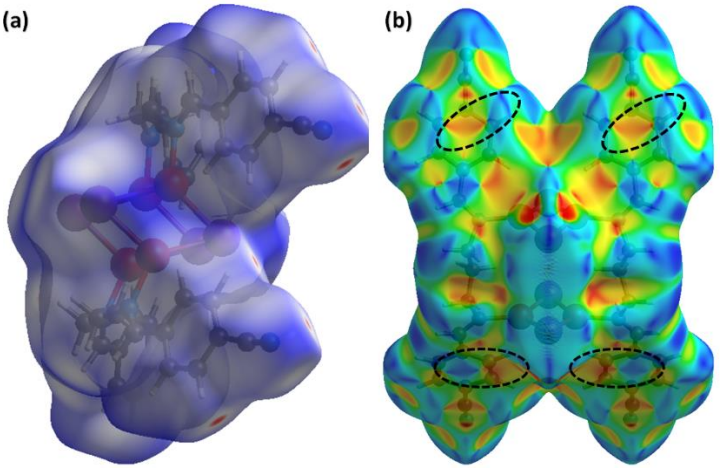

Fig. 7. Hirshfeld surface designed over (a) normalized distances and (b) shape index.

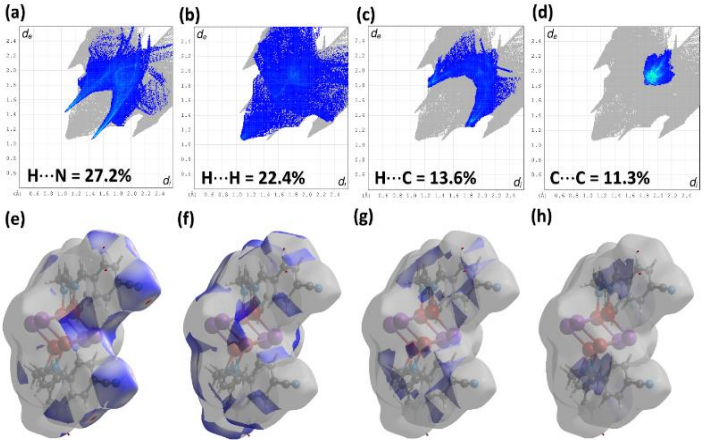

Fig. 8. 2D finger plots of the top four interatomic contacts (a-d) and associated surfaces (e-h).

Table 4. Enrichment Ratio for the Pairs of Chemical Species in **[Cu$_2$(L^{4CN})μ$_2$-I]$_2$** with Random Contacts Greater than 0.98

	Atom	**H**	**C**	**N**	**I**	**Cu**
Contact%	**H**	22.4	13.6	27.2	19.1	0.5
	C	13.6	11.3	4		
	N	27.2	4	0.2		
	I	19.1			1.7	
	Cu	0.5				
Surface%		52.6	20.1	15.8	11.25	0.25
	Atom	**H**	**C**	**N**	**I**	**Cu**
Random contacts%	**H**	27.67				
	C	21.15	4.04			
	N	16.62	6.35	2.50		
	I	11.84	4.52	3.56	1.27	
	Cu	0.26	0.10	0.08	0.06	0.00
	Atom	**H**	**C**	**N**	**I**	**Cu**
Enrichment ratio	**H**	0.81				
	C	0.64	2.80			
	N	1.64	0.63	0.08		
	I	1.61	0.00	0.00	1.34	
	Cu		0.00			

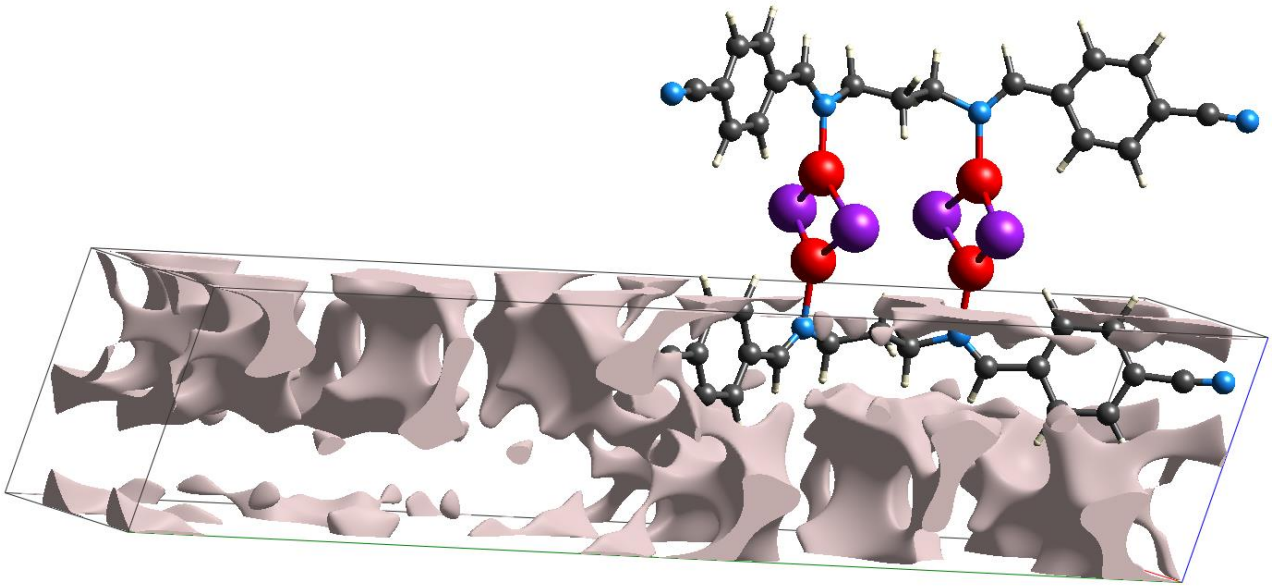

Fig. 9. Isosurfaces of voids in **[Cu$_2$(L^{4CN})μ$_2$-I]$_2$**.

Voids are referred to as predicting the mechanical stability of the crystal, which has an inverse relation to mechanical stability. Tuner *et al's*. [39] methodology is employed for voids calculation of **[Cu$_2$(L^{4CN})μ$_2$-I]$_2$**. The calculated void volume is 263.83 Å^3, which represents 11.9% voids. As most of the unit cell space is occupied by molecules, it indicates that the crystal is likely to exhibit good mechanical stability and can withstand considerable stress without undergoing permanent deformation (Fig. 9).

Computational Details and Electronic Structure Analysis

Geometry optimization. The geometrical structure of the complex was successfully optimized using density functional theory (DFT) as implemented in the Gaussian 09 software package [40]. B3LYP functional [41] coupled with the def2-TZVP basis set was employed for all the calculations for all atoms [42]. Figure 10 shows optimized structures of the complex, with clear designations of symbols for atoms. Table 2 presents a comparison of the bond lengths and bond angles of the optimized complex with those obtained experimentally. Specifically, the calculated bond lengths for I_2–Cu_2, I_1–Cu_1, I_2–Cu_2, I_2–Cu_1, Cu_1–N_2, and Cu_2–N_3 were 2.64, 2.64, 2.61, 2.61, 2.03, and 2.03 Å, respectively. On the basis of these, the results favored the proposed geometry of the **$[Cu_2(L^{4CN})\mu_2\text{-}I]_2$** complex and showed a good agreement with experimental data. This optimized structure served as the groundwork for additional computational studies, from which interaction parameters were derived. Advanced quantum chemical methods were employed to explore the electronic behavior of the molecular system. The highest occupied molecular orbital (HOMO) and lowest unoccupied molecular orbital (LUMO) contour diagrams were generated using the GaussView program. Molecular electrostatic potential (MEP) maps were carefully analyzed and graphically represented. Additionally, natural bond orbital (NBO) calculations were performed using the NBO 6.0 program [43] to understand the electronic framework and bonding characteristics of the system.

Molecular orbitals. Molecular orbitals of the HOMO and LUMO types were calculated from the optimized geometry of the complex. The related orbital energy levels (in eV) and percentage contributions of the metal centers and coordinated ligand are shown in Fig. 11. The corresponding HOMO–LUMO energy level diagram of the complex is also illustrated in the same figure. In the case of the **$[Cu_2(L^{4CN})\mu_2\text{-}I]_2$** complex, the HOMO is localized at the ligand (56%) with a small contribution from the Cu centers (44%). Similarly, the LUMO is almost localized over the ligand (98%) with very little contribution from the metal centers (2%). HOMO–LUMO energy gap of the complex was found to be 2.56 eV, as shown in Fig. 11.

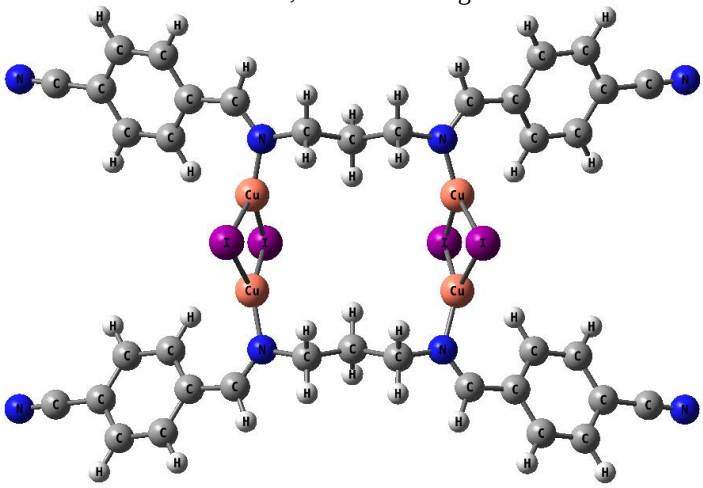

Fig. 10. Optimized structure of **$[Cu_2(L^{4CN})\mu_2\text{-}I]_2$** with symbol of atoms.

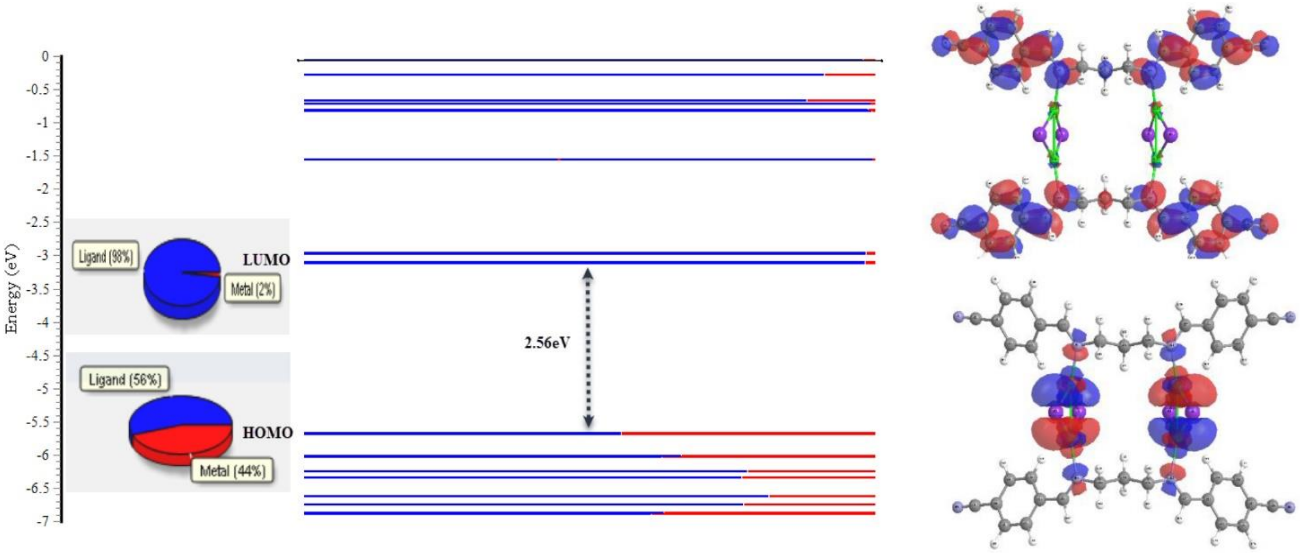

Fig. 11. Calculated molecular orbital energy level diagrams and visual representations of HOMO and LUMO distributions for the complex are presented. Contributions from the ligand in **$[Cu_2(L^{4CN})\mu_2\text{-}I]_2$**'s diagram are indicated by blue lines and metal centers' contributions by red lines.

Molecular electrostatic potential. Molecular electrostatic potential (MEP) analysis provides valuable information regarding the reactive sites of molecules. The MEP map displays positive electrostatic regions (blue) prone to nucleophilic attack and negative regions (red) susceptible to electrophilic interactions. The MEP surface of the **[Cu$_2$(L^{4CN})μ$_2$-I]$_2$** complex was calculated and is shown in Fig. 12a. Electron-rich areas around electronegative atoms, particularly iodine and nitrogen, are identified as likely sites of activity to interact with positively charged metal ions. Additionally, an electron density contour plot for the **[Cu$_2$(L^{4CN})μ$_2$-I]$_2$** complex is shown in Fig. 12b, where red and green indicate areas of negative and positive charge density, respectively. The regions where electrons are more localized, usually around electronegative atoms or bonding areas, appear red, while green areas indicate lower electron density, typically near metal centers or less electronegative atoms. This electron density map is crucial in understanding bonding interactions, charge delocalization, and the electronic environment within the complex.

NBO analysis. The natural population analysis (NPA) and electronic configuration data in Table 5 provide valuable insights into the complex's electronic properties, calculated using the B3LYP/Def2-TZVP method, which is known for its reliability in modeling transition metal systems. Copper atoms, with partial positive charges around +0.33, reflect their role as metal centers that often act as electron acceptors in coordination complexes. These positive charges indicate a degree of electron density withdrawal by coordinating ligands, a behavior characteristic of Cu(I) centers depending on their coordination environment. The iodide atoms exhibit significant negative partial charges, ranging from -0.41 to -0.45, underscoring their role as electron-rich halides that donate lone pair electrons to the metal centers, thereby stabilizing the complex through both ionic and covalent interactions. Nitrogen atoms, commonly key donor sites in ligand frameworks, display moderately negative charges between -0.28 and -0.43, reflecting their involvement in electron donation and coordination to the metal centers. This interaction contributes to a balanced ligand field and facilitates optimized bonding within the complex.

Carbon atoms exhibit a range of small positive and negative charges depending on their bonding situations within the organic ligand structure, which reflects subtle electron delocalization patterns and resonance effects affecting the overall electronic environment. Copper centers maintain nearly fully occupied core orbitals, consistent with their atomic nature, while valence shells are dominated by a nearly filled 3d subshell (~9.89 electrons), complemented by partial occupation of 5s and 4p orbitals. This distribution suggests a substantial d-electron contribution to bonding, with the 5s and 4p orbitals facilitating covalent interactions and electron density delocalization.

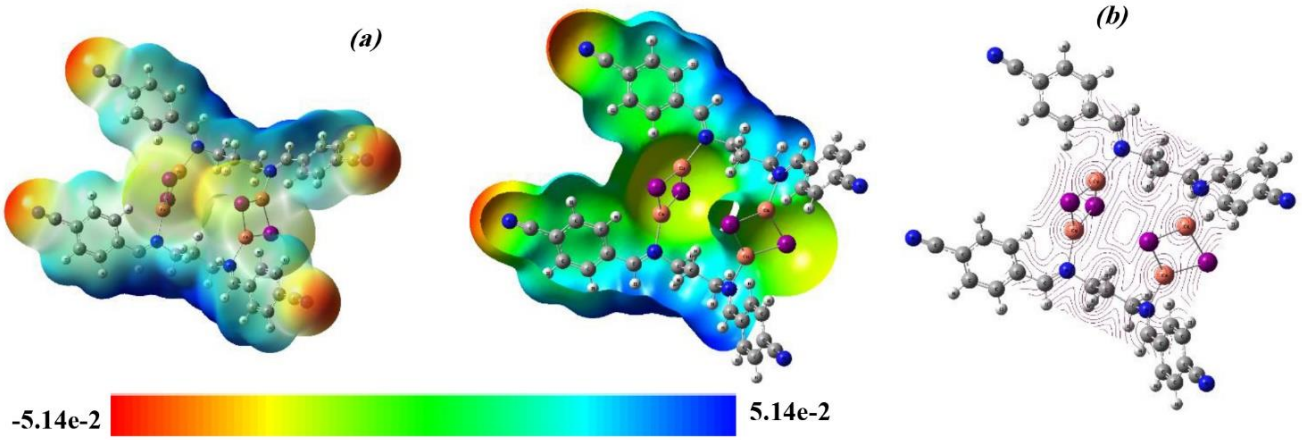

Fig. 12. (a) Electrostatic potential diagram of the **[Cu$_2$(L^{4CN})μ$_2$-I]$_2$** complex, on a color gradient and included scale. (b) Electron density contour plot of the **[Cu$_2$(L^{4CN})μ$_2$-I]$_2$** complex, red for negative charge regions and green for positive charge regions.

Table 5. An Overview of the Natural Population Analysis and the Inherent Electronic Configuration of the Complex, Derived through Calculations Utilizing the B3LYP Functional in Conjunction with the Def2-TZVP Basis Set

Atom	Charge	Natural population				Natural Electron Configuration
		Core	Valence	Rydberg	Total	
I1	-0.41194	45.99838	7.39982	0.01374	53.41194	[core]$5s^{1.91}5p^{5.49}5d^{0.01}$
Cu2	0.33384	17.99744	10.65358	0.01513	28.66616	[core]$5s^{0.39}3d^{9.89}4p^{0.37}5d^{0.01}$
N3	-0.43241	1.99933	5.3973	0.03578	7.43241	[core]$2s^{1.35}2p^{4.05}3p^{0.02}3d^{0.01}$
N4	-0.28227	1.99961	5.25504	0.02763	7.28227	[core] $2s^{1.59}2p^{3.67}3d^{0.01}$
C5	0.26484	1.99925	3.70608	0.02983	5.73516	[core]$2s^{0.85}2p^{2.85}3s^{0.01}3p^{0.02}$
C6	-0.14715	1.99886	4.12993	0.01836	6.14715	[core]$2s^{0.92}2p^{3.21}3p^{0.01}$
C7	-0.15599	1.99911	4.13831	0.01857	6.15599	[core]$2s^{0.97}2p^{3.17}3p^{0.01}3d^{0.01}$
C9	-0.15936	1.99914	4.14242	0.01781	6.15936	[core]$2s^{0.97}2p^{3.17}$ $3p^{0.01}$
C11	-0.10152	1.99905	4.08269	0.01978	6.10152	[core]$2s^{0.93}2p^{3.16}3p^{0.01}$
C12	-0.15086	1.99905	4.13336	0.01845	6.15086	[core]$2s^{0.97}2p^{3.16}3p^{0.01}3d^{0.01}$
C14	-0.14459	1.99912	4.12744	0.01804	6.14459	[core]$2s^{0.85}2p^{2.85}3s^{0.01}3p^{0.02}$
C16	0.14991	1.99926	3.82917	0.02166	5.85009	[core]$2s^{0.97}2p^{3.16}3p^{0.01}3d^{0.01}$
C18	-0.22054	1.99935	4.20402	0.01716	6.22054	[core]$2s^{1.03}2p^{3.17}$ $3p^{0.01}$
C21	-0.39454	1.99936	4.38194	0.01324	6.39454	[core]$2s^{1.06}2p^{3.32}$ $3p^{0.01}$
N24	-0.43233	1.99933	5.39721	0.03578	7.43233	[core]$2s^{1.35}2p^{4.05}3p^{0.02}3d^{0.01}$
N25	-0.28226	1.99961	5.25503	0.02763	7.28226	[core]$2s^{1.59}2p^{3.67}$ $3p^{0.02}$
C26	0.26484	1.99925	3.70608	0.02983	5.73516	[core]$2s^{0.85}2p^{2.85}3s^{0.01}3p^{0.02}$
C27	-0.14715	1.99886	4.12994	0.01836	6.14715	[core]$2s^{0.92}2p^{3.21}3p^{0.01}$
C28	-0.15599	1.99911	4.13831	0.01857	6.15599	[core]$2s^{0.97}2p^{3.17}3p^{0.01}3d^{0.01}$
C30	-0.15936	1.99914	4.14241	0.01781	6.15936	[core]$2s^{0.97}2p^{3.17}$ $3p^{0.01}$
C32	-0.10151	1.99905	4.08268	0.01978	6.10151	[core]$2s^{0.93}2p^{3.16}3p^{0.01}$
C33	-0.15071	1.99905	4.13322	0.01845	6.15071	[core]$2s^{0.97}2p^{3.16}3p^{0.01}3d^{0.01}$
C35	-0.14459	1.99912	4.12743	0.01804	6.14459	[core]$2s^{0.97}2p^{3.16}3p^{0.01}3d^{0.01}$
C37	0.14987	1.99926	3.82921	0.02166	5.85013	[core]$2s^{0.97}2p^{3.16}3p^{0.01}3d^{0.01}$
C39	-0.22046	1.99935	4.20394	0.01717	6.22046	[core]$2s^{1.03}2p^{3.17}$ $3p^{0.01}$
Cu42	0.33339	17.99744	10.65402	0.01514	28.66661	[core]$5s^{0.39}3d^{9.89}4p^{0.37}5d^{0.01}$
N43	-0.28226	1.99961	5.25503	0.02763	7.28226	[core]$2s^{1.59}2p^{3.67}3d^{0.02}$
N44	-0.43234	1.99933	5.39722	0.03578	7.43234	[core]$2s^{1.39}2p^{4.05}3p^{0.02}3d^{0.01}$
C45	0.26484	1.99925	3.70608	0.02983	5.73516	[core]$2s^{0.85}2p^{2.85}3s^{0.01}3p^{0.02}$
C46	-0.14715	1.99886	4.12994	0.01836	6.14715	[core]$2s^{0.92}2p^{3.21}3p^{0.01}$
C47	-0.14459	1.99912	4.12743	0.01804	6.14459	[core]$2s^{0.97}2p^{3.16}3p^{0.01}3d^{0.01}$
C49	-0.15074	1.99905	4.13325	0.01845	6.15074	[core]$2s^{0.97}2p^{3.16}3p^{0.01}3d^{0.01}$
C51	-0.10151	1.99905	4.08267	0.01978	6.10151	[core]$2s^{0.93}2p^{3.16}3p^{0.01}$
C52	-0.15936	1.99914	4.14242	0.01781	6.15936	[core]$2s^{0.97}2p^{3.16}3p^{0.01}3d^{0.01}$
C54	-0.15599	1.99911	4.13831	0.01857	6.15599	[core]$2s^{0.97}2p^{3.17}3p^{0.01}3d^{0.01}$
C56	0.14987	1.99926	3.82921	0.02166	5.85013	[core]$2s^{0.93}2p^{2.9}3s^{0.01}3p^{0.01}$
C58	-0.22048	1.99935	4.20396	0.01717	6.22048	[core]$2s^{1.03}2p^{3.17}$ $3p^{0.01}$
C61	-0.39454	1.99936	4.38194	0.01324	6.39454	[core]$2s^{1.06}2p^{3.32}3d^{0.01}$
N64	-0.28227	1.99961	5.25503	0.02763	7.28227	[core]$2s^{1.06}2p^{3.32}3d^{0.01}$
N65	-0.43241	1.99933	5.39729	0.03578	7.43241	[core]$2s^{1.35}2p^{4.05}3p^{0.02}3d^{0.01}$
C66	0.26484	1.99925	3.70608	0.02983	5.73516	[core]$2s^{0.85}2p^{2.85}3s^{0.01}3p^{0.02}$
C67	-0.14716	1.99886	4.12994	0.01836	6.14716	[core]$2s^{0.92}2p^{3.21}3p^{0.01}$
C68	-0.14459	1.99912	4.12744	0.01804	6.14459	[core]$2s^{0.97}2p^{3.16}3p^{0.01}3d^{0.01}$
C70	-0.15089	1.99905	4.13339	0.01845	6.15089	[core]$2s^{0.97}2p^{3.16}3p^{0.01}3d^{0.01}$
C72	-0.10151	1.99905	4.08268	0.01978	0.7711	[core]$2s^{0.93}2p^{3.16}3p^{0.01}$
C73	-0.15936	1.99914	4.14242	0.01781	6.10151	[core]$2s^{0.97}2p^{3.17}3p^{0.01}$
C75	-0.15599	1.99911	4.1383	0.01857	6.15936	[core]$2s^{0.97}2p^{3.17}3p^{0.01}3d^{0.01}$
C77	0.1499	1.99926	3.82918	0.02166	6.15599	[core]$2s^{0.93}2p^{2.9}3s^{0.01}3p^{0.02}$
C79	-0.22053	1.99935	4.20401	0.01716	5.8501	[core]$2s^{1.03}2p^{3.17}3p^{0.01}$
I82	-0.44816	45.99851	7.43756	0.0121	6.22053	[core]$5s^{1.91}5p^{5.52}5d^{0.01}$
I83	-0.41195	45.99838	7.39984	0.01373	53.44816	[core]$5s^{1.91}5p^{5.49}5d^{0.01}$
Cu84	0.33329	17.99744	10.65413	0.01514	53.41195	[core]$5s^{0.39}3d^{9.89}4p^{0.37}5d^{0.01}$
Cu85	0.3338	17.99744	10.65363	0.01513	28.66671	[core]$5s^{0.39}3d^{9.89}4p^{0.37}5d^{0.01}$
I86	-0.44803	45.99851	7.43742	0.0121	28.6662	[core]$5s^{1.91}5p^{5.52}5d^{0.01}$

The occupation of these orbitals matches expected electronic configurations for copper centers bound to ligands with varying electronegativities, reinforcing the complex's electronic stability. Nitrogen atoms show primarily filled 2s and 2p orbitals, confirming their expected role as electron donors with lone pairs engaging in coordination bonds. Carbon atoms similarly reflect strong 2s and 2p occupation characteristic of covalent frameworks, with minor contributions from higher orbitals suggesting subtle polarization effects. Iodine atoms display nearly full 5s and 5p orbitals, accompanied by minimal occupancy of d orbitals, reflecting their electron-rich and relatively inert character within the complex, adding to the stability through lone pair donation and polarization. The electron-rich iodines and nitrogens enhance the covalent character of metal ligand bonding by donating electron density into the copper's partially vacant orbitals, leading to stable coordination environments.

Table 6, which presents the second-order perturbation analysis of the Fock matrix in the NBO basis for the complex calculated at the B3LYP/Def2-TZVP level, focuses on the significant donor-acceptor interactions characterized by their stabilization energies $E^{(2)}$. The second-order perturbation analysis offers critical insights into the electronic delocalization and donor-acceptor interactions that govern the stability and bonding framework of the complex. Additionally, several antibonding lone pair orbitals of copper, such as LP*(6), LP*(7), and LP*(8), serve as key acceptors, with LP(1) I_1 donating strongly toward these orbitals, manifesting stabilization energies ranging from moderate (~16.76 kcal mol^{-1}) to very high (~82.59 kcal mol^{-1}), emphasizing multifaceted copper-iodine bonding contributing prominently to the complex's electronic architecture. The copper centers also feature extensive intrametal and ligand-to-metal interactions. Lone pairs on copper atoms (LP*(5), LP*(6), and LP*(7)) donate electron density to antibonding orbitals of neighboring atoms or ligands, further stabilizing the complex. This interplay is reflected in several donor–acceptor pairs with notable stabilization energies; for instance, LP*(7) Cu2 and LP*(8) Cu42 exhibit strong mutual interactions exceeding 200 kcal mol^{-1}, suggesting significant metal-to-metal communication or cooperative effects that enhance the complex's overall stability. The presence of strong acceptor orbitals on copper highlights its electron-accepting ability, consistent with the partial positive charge observed in the population analysis. Similarly, π–π* interactions within the conjugated ligand framework show significant delocalization, where π orbitals from C=C bonds donate into neighboring π* antibonding orbitals, enhancing the ligand's electronic stability. These π→π* interactions yield very high stabilization energies, frequently over 200 kcal mol^{-1}, as seen for C_{72}-C_{73}→C_{68}-C_{70} and C_{30}-C_{32}→C_{33}-C_{35}, reflecting extensive electron delocalization across the ligand backbone. Such π conjugation is vital for electronic communication throughout the ligand system, affecting optical, electronic, and reactive properties of the complex. Nitrogen atoms contribute with lone pairs donating to metal-centered antibonding orbitals with appreciable energies (*e.g.*, LP(1) N_{65}→LP*(8) Cu_{85} with 45.83 kcal mol^{-1}), underscoring the pivotal role of nitrogen as a metal-coordinating donor, reinforcing the coordination sphere. These second-order interactions, although lower in energy than metal-ligand interactions, contribute cumulatively to the fine-tuning of the molecular framework. The presence of multiple overlapping donor-acceptor pairs involving lone pairs on iodine and copper interacting reciprocally also hints at charge redistribution pathways, possibly relevant for electronic excitations or chemical reactivity. Smaller orbital energy gaps and larger Fock matrix elements correlate with stronger donor-acceptor interactions, as observed in multiple LP→LP* or LP→σ* pairs involving copper centers and halides, supporting the notion of electron sharing and covalency. Notably, the extremely high stabilization energies exceeding 200 kcal mol^{-1} between LP*(7) and LP*(8) orbitals on copper atoms point to significant orbital overlap and electronic communication inside the metal-cluster or metal-ligand core, essential for the complex's redox and catalytic profiles.

Table 6. A Second-order Perturbation Analysis of the Fock Matrix within the Framework of the NBO Basis for the Complex, Executed with the B3LYP Functional and the Def2-TZVP Basis Set. The Stabilization Energies $E^{(2)}$ (Expressed in kcal mol^{-1}) Elucidate the most Prominent Donor-acceptor Interactions

Donor (i)	Type	Acceptor (j)	Type	$E^{(2)a}$	E(j) – E(i)[b]	F(i,j)[c]
I_1-Cu_2	σ^*	LP* (7) Cu_2		21.06	0.20	0.161
I_1-Cu_2	σ	LP* (6) Cu_2		82.59	0.46	0.183
LP* (7) Cu_2		LP* (8) Cu_{42}		236.13	0.04	0.239
LP (1) N_3		LP* (7) Cu_2		44.01	0.86	0.177
LP (4) I_{86}		LP* (6) Cu_{84}		51.81	0.53	0.154
LP (4) I_{86}		LP* (6) Cu_{85}		44.11	0.40	0.118
LP* (7) Cu_{84}		LP* (8) Cu_{85}		235.42	0.04	0.239
I_{83}-Cu_{84}	σ	LP* (6) Cu_{85}		82.64	0.46	0.183
I_{83}-Cu_{84}	σ	LP* (7) Cu_{85}		23.29	0.67	0.112
I_{83}-Cu_{84}	σ*	LP* (7) Cu_{84}		21.03	0.20	0.161
LP* (6) Cu_{84}		I_{83}-Cu_{84}	σ*	63.20	0.05	0.123
LP* (4) I_{82}		LP* (6) Cu_2		44.31	0.40	0.119
LP* (4) I_{82}		LP* (7) Cu_{42}		26.33	0.61	0.119
LP* (4) I_{82}		LP* (6) Cu_2		51.55	0.53	0.153
LP (1) N_{65}		LP* (8) Cu_{85}		45.83	0.91	0.185
C_{72}-C_{73}	π^*	C_{68}-C_{70}	π^*	223.93	0.01	0.078
C_{67}-C_{75}	π^*	C_{68}-C_{70}	π^*	208.21	0.01	0.077
C_{46}-C_{54}	π^*	C_{47}-C_{49}	π^*	208.3	0.01	0.077
C_{72}-C_{73}	π	N_{65}-C_{77}	π^*	20.50	0.26	0.070
C_{72}-C_{73}	π	C_{67}-C_{75}	π^*	21.10	0.27	0.068
C_{68}-C_{70}	π	C_{67}-C_{75}	π^*	20.49	0.27	0.067
C_{68}-C_{70}	π	C_{72}-C_{73}	π^*	20.42	0.27	0.067
C_{67}-C_{75}	π	C_{72}-C_{73}	π^*	20.29	0.28	0.067
C_{51}-C_{52}	π	N_{44}-C_{56}	π^*	20.51	0.26	0.070
C_{51}-C_{52}	π	C_{46}-C_{54}	π^*	21.10	0.27	0.068
C_{47}-C_{49}	π	C_{46}-C_{54}	π^*	20.49	0.27	0.067
C_{47}-C_{49}	π	C_{51}-C_{52}	π^*	20.42	0.27	0.067
C_{46}-C_{54}	π	C_{47}-C_{49}	π^*	20.29	0.28	0.067
LP (1) N_{44}		LP* (6) Cu_{42}		45.90	0.91	0.185
LP* (6) Cu_{42}		I_1 -Cu_2	σ*	24.38	0.18	0.119
LP (1) N_{24}		LP* (7) Cu_{84}		44.14	0.87	0.177
C_{30}-C_{32}	π	C_{33}-C_{35}	π^*	223.98	0.01	0.078
C_{27}-C_{28}	π	C_{33}-C_{35}	π^*	208.31	0.01	0.077
C_9-C_{11}	π	C_{12}-C_{14}	π^*	223.78	0.01	0.078

[a]$E^{(2)}$ = Stabilization energy of hyperconjugative interaction. Higher values indicate stronger interactions. [b]Energy difference between donor (i) and acceptor (j) NBO orbitals. Smaller differences tend to favor stronger interactions. [c]F(i, j) is the Fock matrix element between i and j NBO orbitals, indicating the overlap or coupling strength.

Molecular Docking Calculations

Molecular docking studies have become an essential tool for investigating how copper complexes bind with biological partners such as DNA and proteins [44-46]. These computational studies provide precise details about the binding mode, affinity, and key intermolecular interactions that determine the stability and specificity of copper complex-biomolecule complexes. Software-based calculations offer systematic insights into how these complexes interact, including their binding modes, affinities, and the critical intermolecular forces involved. For example, docking simulation of copper complex with DNA often shows intercalative or groove-binding modes, where the complexes interact with nucleobases *via* hydrogen bonds,

electrostatic forces, and hydrophobic contacts, thereby impacting DNA's structure and function. Likewise, docking studies against proteins like BSA help identify preferred binding sites and the nature of interactions with amino acid residues, which is crucial for understanding the pharmacokinetics and bioavailability of copper-based drugs [47-49].

DNA molecular docking. In this research, the binding of the complex **$[Cu_2(L^{4CN})\mu_2\text{-}I]_2$** with DNA and BSA is thoroughly studied employing AutoDock Vina (version 1.1.2) software [50]. The employed DNA structure (PDB ID: 423D) was for the d(ACCGACGTCGGT)$_2$ sequence, whereas the BSA structure (PDB ID: 4F5S) was derived from the Protein Data Bank, with resolution of 1.60 Å and 2.47 Å, respectively [51]. The complex structure was determined from X-ray diffraction data and further optimized using DFT calculations. Blind docking (BD) was employed to predict potential binding sites and identify ligand contact points across the entire surfaces of DNA and BSA [52-54]. The binding affinities of the complex toward DNA and BSA were assessed through BD studies, which revealed key structural features of the biomolecules and provided a basis for subsequent focused docking experiments. Grid boxes of 66 × 84 × 76 Å^3 for DNA and 84 × 94 × 90 Å^3 for BSA (x, y, and z directions) were fixed. The calculated lowest binding free energies (ΔG_b) indicate strong binding interactions with particular values provided in Table 7. Figures 13 and 14 illustrate the binding sites and key interactions of **$[Cu_2(L^{4CN})\mu_2\text{-}I]_2$** with DNA, highlighting the significantly involved nucleobases and the nature of their interactions, which are further detailed in the supplementary interaction schemes. Figure 13a illustrates the docking pose with widespread interaction with specific DNA bases, while Figure 13b illustrates a 3D representation of key hydrogen bond interactions. Figure 14a represents a 2D representation of **$[Cu_2(L^{4CN})\mu_2\text{-}I]_2$** interactions in which hydrogen bonds, as well as hydrophobic contacts (red dotted lines), are shown.

The results confirm that the **$[Cu_2(L^{4CN})\mu_2\text{-}I]_2$** complex predominantly interacts within the major grooves of DNA. This finding aligns with the structural characteristics of DNA, where the major groove is wider and deeper than the narrower minor groove, providing more accessible binding sites for larger ligands.

Table 7. Theoretical Free Energy of Binding ($\Delta G°$, kcal mol^{-1}) and Binding Constant (K_b) of the Complex with DNA, Calculated by AutoDock Vina

Compound	$\Delta G°_b$	K_b	$\Delta G°_b$	K_b
	For DNA		For BSA	
$[Cu_2(L^{4CN})\mu_2\text{-}I]_2$	-9.9	1.94×10^7	-8.6	2.14×10^6

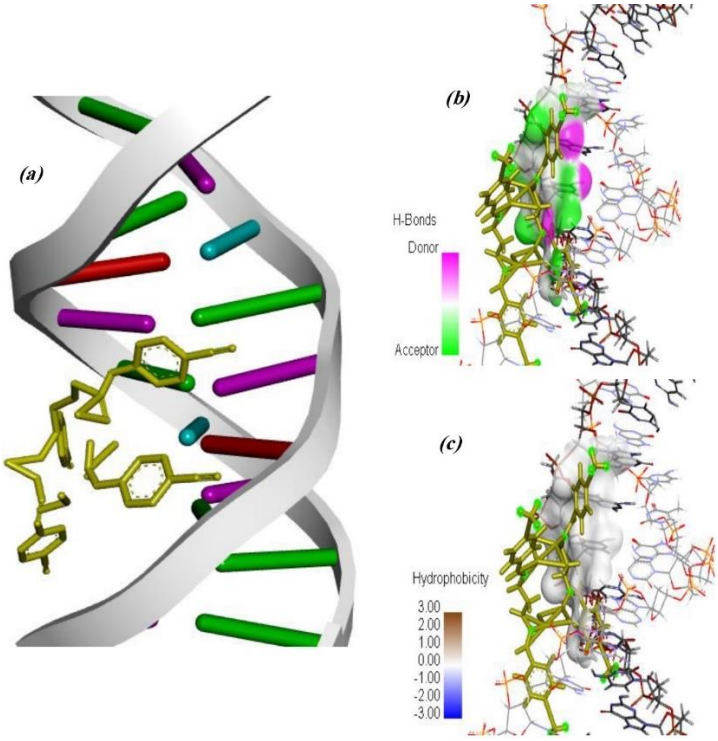

Fig. 13. (a) Docking position of the **$[Cu_2(L^{4CN})\mu_2\text{-}I]_2$** complex at the DNA active site; (b) primary H-bond region interaction with DNA bases; (c) hydrophobic interaction region.

BSA molecular docking. A grid box of 84 × 94 × 90 Å^3 was defined along the x, y, and z axes, and a constant grid spacing of 0.375 Å was employed for BSA and **$[Cu_2(L^{4CN})\mu_2\text{-}I]_2$** docking studies. Binding constants (K_b) for the DNA-BSA complex were calculated from the equation $\Delta G°_b = -RT \ln K_b$, and their values are presented in Table 7. Gibb´s free energy values ($\Delta G°_b$) represent spontaneous binding since they are negative. The binding constants quantify the strength of interaction, with higher values indicating stronger affinities.

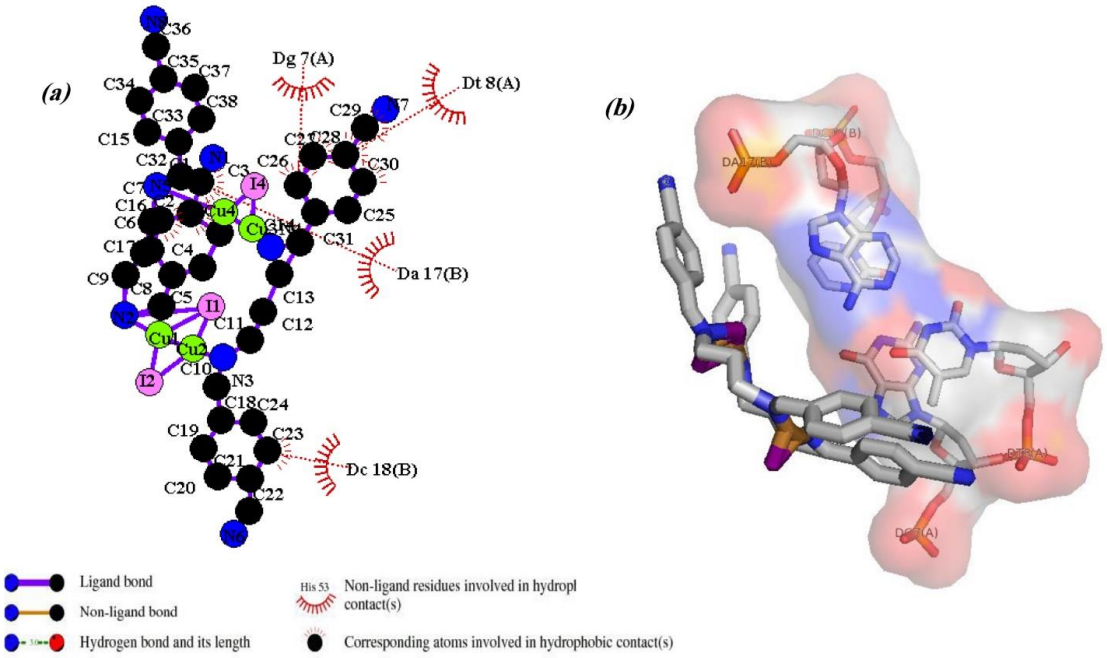

Fig. 14. (a) 2D docking position of the **[Cu₂(L^{4CN})μ₂-I]₂** complex featuring hydrophobic contacts with DNA bases; (b) 3D interaction view.

Figures 15 and 16 display the docking poses and significant interactions of **[Cu₂(L^{4CN})μ₂-I]₂** with BSA. The free binding energy ($\Delta G°_b$) of these interactions is provided in Table 7. The binding interactions between the **[Cu₂(L^{4CN})μ₂-I]₂** complex and BSA are illustrated in Fig. 15. Figure 15a depicts the overall binding pose, while Fig. 15b shows the hydrogen bond region in the active site. Significant hydrophobic interactions between BSA residues and the complex at the active site are depicted in Fig. 15c. Figure 16 shows 2D and 3D representations of **[Cu₂(L^{4CN})μ₂-I]₂** interactions with BSA, presenting hydrophobic contacts (red dotted lines). The two-dimensional interaction map (Fig. 16a) illustrates all types of interactions between the ligand and the amino acid residues of BSA at the active site.

According to their calculated free binding energies and binding constants, theoretical dockings for the Cu(I) Schiff base complex **[Cu₂(L^{4CN})μ₂-I]₂** indicate strong and spontaneous bindings with both DNA and BSA. The Gibb´s free energy values were calculated to be -9.9 kcal mol^{-1} for DNA and -8.6 kcal mol^{-1} for BSA, corresponding to binding constants of 1.94×10^7 and 2.14×10^6, respectively. These results align with experimental studies on similar Cu(I) or Cu(II) Schiff base complexes, which typically report DNA and BSA binding constants ranging from 10^5 to 10^7 for strong binders. The negative $\Delta G°$ values confirm the spontaneous nature of these interactions, consistent with the docking-derived results for **[Cu₂(L^{4CN})μ₂-I]₂** [55-58].

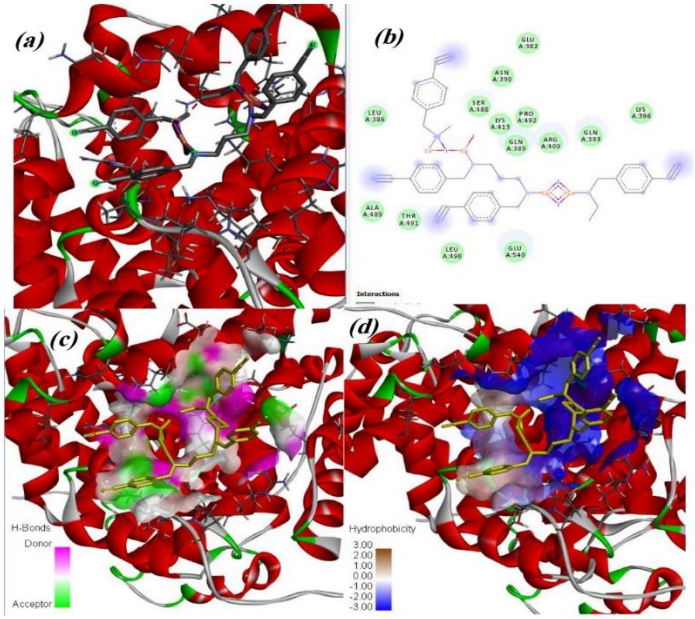

Fig. 15. (a) Binding interaction between **[Cu₂(L^{4CN})μ₂-I]₂** and BSA; (b) Hydrogen bond interaction network between **[Cu₂(L^{4CN})μ₂-I]₂** and BSA; (c) Most significant hydrophobic interactions between BSA residues and **[Cu₂(L^{4CN})μ₂-I]₂** at the active site.

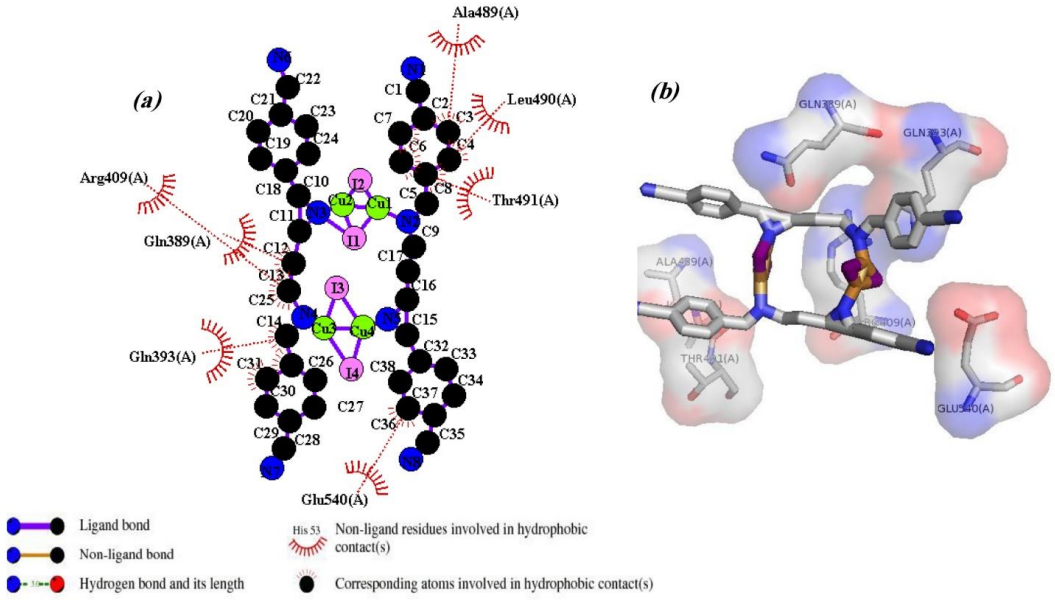

Fig. 16. (a) Two-dimensional graph of all types of interactions between **$[Cu_2(L^{4CN})\mu_2\text{-}I]_2$** and BSA amino acids at the active site, with hydrophobic interactions indicated by red dotted lines; (b) Three-dimensional perspective of BSA residues interacting with **$[Cu_2(L^{4CN})\mu_2\text{-}I]_2$**.

CONCLUSIONS

Herein, a new Salpn-type Schiff base Cu(I) complex has been synthesized and characterized using various spectroscopic techniques. Moreover, the crystal structure was determined using single-crystal X-ray diffraction, revealing that the Schiff base ligand contains four imine groups, all of which participate in coordination with copper atoms. The resulting structure is a tetranuclear copper complex, with each copper center exhibiting a distorted trigonal planar coordination geometry. Solid state assembly is stabilized by C–H···N bonding along with π···π and C–N···π interactions. Hirshfeld surface analysis concluded that H···N, H···H, H···C, and C···C are the top four contributors to the stabilization of the solid-state assembly. MO, MEP, NBO, and NPA calculations were carried out to gain deeper insights into the electronic structure and bonding characteristics of the molecular system. The detailed NPA and natural electron configuration analysis highlights a finely balanced electronic structure within the complex, where charge distribution and orbital occupations collectively stabilize metal-ligand interactions. The positive charges at copper centers, coupled with negative charges on donor atoms, underline the charge transfer mechanisms fundamental to coordination chemistry. The predominance of filled and nearly filled orbitals in the ligand supports its role in electronically stabilizing the metal centers, while subtle variations in electron density across the carbon atoms highlight the complexity of the molecular architecture. These electronic features not only confirm the validity of the computational approach employed but also provide a rich framework to rationalize chemical properties and reactivity, laying the groundwork for further experimental and theoretical exploration of related complexes. The second-order perturbation results consolidate and complement the earlier natural population and electronic configuration analyses by defining not just electron densities but electronic flow pathways and stabilization mechanisms. Molecular docking was utilized to explore potential sites of binding and interactions between the optimized complex and biomolecules such as DNA and BSA. The most stable sites of binding of the complex with DNA were successfully identified. In addition, BSA contacts were investigated, which showed significant contacts at the intended active sites. These findings are crucial in identifying the biochemical processes impacted by these metal complexes.

Appendix A. Supplementary data

CCDC number 2450527 contains the supplementary crystallographic data for **$[Cu_2(L^{4CN})\mu_2\text{-}I]_2$**. These data can be obtained free of charge *via* http://www.ccdc.cam.ac.uk/conts/retrieving.html, or from the Cambridge Crystallographic Data Center, 12 Union Road, Cambridge CB2 1EZ, UK; fax: (+44) 1223-336-033; or e-mail: deposit@ccdc.cam.ac.uk.

REFERENCES

[1] Sivaraman, G.; Iniya, M.; Anand, T.; Kotla, N. G.; Sunnapu, O.; Singaravadivel, S.; Gulyani, A.; Chellappa, D., Chemically diverse small molecule fluorescent chemosensors for copper ion. *Coord. Chem. Rev.* **2018**, *357*, 50-104, DOI: 10.1016/j.ccr.2017.11.020.

[2] Yaşar, Ü.; Gönül, İ.; Türkeş, C.; Demir, Y.; Beydemir, Ş., Transition-metal complexes of bidentate Schiff-base ligands: In vitro and in silico evaluation as non-classical carbonic anhydrase and potential acetylcholinesterase inhibitors. *ChemistrySelect* **2021**, *6*, 7278-7284, DOI: 10.1002/slct.202102082.

[3] Ismaeel, M.; Parveen, B.; Dogar, S. S.; Aftab, K.; Abbas, K.; Munawar, K. S., Comparing green and conventional methods for Schiff base synthesis and unveiling environmental stability applications: A review. *J. Coord. Chem.* **2024**, *77*, 921-959, DOI: 10.1080/00958972.2024.2362344.

[4] Jawaria, R.; Khalid, M.; Munir, S.; Shafiq, I.; Barga, A. A.; Munawar, K. S.; Alrashidi, K. A.; Ahmed, S., Synthesis, characterization, and DFT insights into non-linear optical properties of ethoxysalicylaldehyde thiosemicarbazone derivatives. *ChemistrySelect* **2025**, *10*, e202403136, DOI: 10.1002/slct.202403136.

[5] Fallah-Mehrjardi, M.; Kargar, H.; Ashfaq, M..; Munawar, K. S., A review of bidentate NN and NO Schiff base ligands and metal complexes. *Inorg. Chim. Acta* **2025**, *587*, 122822, DOI: 10.1016/j.ica.2025.122822.

[6] Kargar, H.; Fallah-Mehrjardi, M.; Moghadam, M.; Yarahmadi, S.; Omidvar, A.; Zare-Mehrjardi, H. R.; Dege, N.; Ashfaq, M.; Munawar, K. S.; Tahir, M. N.; Shahsavari, H. R., Structural and electrochemical properties of a Cu(I) Schiff-base complex: Catalytic application to the synthesis of tetrahydropyrimidine derivatives. *Inorg. Chim. Acta* **2024**, *570*, 122160, DOI: 10.1016/j.ica.2024.122160.

[7] Ogutu, H. F. O.; Saban, W.; Malgas-Enus, R.; Luckay, R. C., Synthesis and characterization of 5- and 7-donor Schiff base ligands and spectroscopic evidence for tautomerism: A crystal structure showing tautomeric forms within one ligand. *J. Mol. Struct.* **2019**, *1185*, 392-402, DOI: 10.1016/j.molstruc.2019.02.054.

[8] Sivaraman, G.; Anand, T.; Chellappa, D., A fluorescence switch for the detection of nitric oxide and histidine and its application in live cell imaging. *ChemPlusChem* **2014**, *79*, 1761-1766, DOI: 10.1002/cplu.201402217.

[9] Swamy, P. C. A.; Sivaraman, G.; Priyanka, R. N.; Raja, S. O.; Ponnuvel, K.; Shanmugpriya, J.; Gulyani, A., Near infrared (NIR) absorbing dyes as promising photosensitizer for photo dynamic therapy. *Coord. Chem. Rev.* **2020**, *411*, 213233, DOI: 10.1016/j.ccr.2020.213233.

[10] Malik M. A.; Dar, O. A.; Gull, P.; Wani, M. Y.; Hashmi, A. A., Heterocyclic Schiff base transition metal complexes in antimicrobial and anticancer chemotherapy. *MedChemComm*. **2018**, *9*, 409-436, DOI: 10.1039/C7MD00526A.

[11] Ahmed, K. Y.; Al-Zinkee, J. M.; Salih, B. D.; Jarullah, A. A.; Alheety. M. A.; Rustagi, S.; Ghotekar. S., Synthesize of α,β-unsaturated Schiff-based complexes for hydrogen storage application. *J. Appl. Organomet. Chem.* **2024**, *4*, 287-295, DOI: 10.48309/jaoc.2024.460226.1198.

[12] Yam, V. W. -W.; Au, V. K. -M.; Leung, S. Y. -L., Light-emitting self-assembled materials based on d^8 and d^{10} transition metal complexes. *Chem. Rev.* **2015**, *115*, 7589-7728, DOI: 10.1021/acs.chemrev.5b00074.

[13] Beheshti, A.; Clegg, W.; Nobakht, V.; Panahi Mehr, M.; Russo, L., Complexes of copper(I) and silver(I) with bis(methimazolyl)borate and dihydrobis(2-mercaptothiazolyl)borate ligands. *Dalton Trans.* **2008**, 6641-6646, DOI: 10.1039/b811369f.

[14] Kobayashi, A.; Kato, M., Stimuli-responsive luminescent copper(I) complexes for intelligent emissive device. *Chem. Lett.* **2017**, *46*, 154-162, DOI: 10.1246/cl.160794.

[15] Benesperi, I.; Singh, R.; Freitag, M., Copper coordination complexes for energy-relevant applications. *Energies* **2020**, *13*, 2198, DOI: 10.3390/en13092198.

[16] Beheshti, A.; Clegg, W.; Mousavi Fard, S. A.; Harrington, R. W.; Nobakht, V.; Russo, L., Synthesis and crystal structures of dimeric W(Mo)/Cu/S and polymeric W/Cu/S neutral clusters with flexible 1,4-bis(3,5-dimethylpyrazol-1-yl)butane as a linker ligand. *Inorg. Chim. Acta* **2011**, *376*, 310-316, DOI: 10.1016/j.ica.2011.06.034.

[17] Beheshti, A.; Nobakht, V.; Behbahanizadeh, S. K.; Abrahams, C. T.; Bruno, G.; Amiri Rudbari, H., Mo(W)/Cu/S coordination polymers based on tetranuclear cubane-like cluster nodes and 1,4-bis(3,5-dimethypyrazol-1-yl)butane flexible ligand. *Inorg. Chim. Acta* **2015**, *437*, 20-25, DOI: 10.1016/j.ica.2015.07.044.

[18] Beheshti, A.; Clegg, W.; Nobakht, V.; Harrington, R. W., Design, synthesis, and structures of two-dimensional copper(I) coordination polymers by variation of co-ligands in a facile one-pot reaction. *Polyhedron* **2014**, *81*, 256-260, DOI: 10.1016/j.poly.2014.06.011.

[19] Tarassoli, A.; Nobakht, V.; Baladi, E.; Carlucci, L.; Proserpio, D. M., Capture of volatile iodine by newly prepared and characterized non-porous $[CuI]_n$-based coordination polymers. *CrystEngComm* **2017**, *19*, 6116-6126, DOI: 10.1039/c7ce01193h.

[20] Baladi, E.; Nobakht, V.; Tarassoli, A.; Proserpio, D. M.; Carlucci, L., Three cationic, nonporous Cu^{I}-coordination polymers: structural investigation and vapor iodine capture. *Cryst. Growth Des.* **2018**, *18*, 7207-7218, DOI: 10.1021/acs.cgd.8b01446.

[21] Caviglia, M.; Li, Z.; Santini, C.; Del Gobbo, J.; Cimarelli, C.; Du, M.; Dolmella, A.; Pellei, M., New Cu(II), Cu(I) and Ag(I) complexes of phenoxy-ketimine Schiff base ligands: Synthesis, structures and antibacterial activity. *Molecules* **2025**, *30*, 1893, DOI: 10.3390/molecules30091893.

[22] Ayare, N. N.; Shukla, V. K.; Sekar, N., Charge transfer and nonlinear optical properties of anthraquinone D-π-A dyes in relation with the DFT based molecular descriptors and perturbational potential. *Comput. Theor. Chem.* **2020**, *1174*, 112712, DOI: 10.1016/j.comptc.2020.112712.

[23] El-Kasaby, R. A.; Al-Farraj, E. S.; Abdou, A.; Abu-Dief, A. M., Synthesis, spectral analysis, physicochemical investigation and biomedical potential of some novel Cu(II), Ru(III) and VO(II) complexes with anthraquinone-based Schiff base supported by DFT and molecular docking insights. *J. Mol. Struct.* **2025**, *1345*, 143010, DOI: 10.1016/j.molstruc.2025.143010.

[24] Kargar, H.; Fallah-Mehrjardi, M.; Moghadam, M.; Omidvar, A.; Zare-Mehrjardi, H. R.; Dege, N.; Ashfaq, M.; Munawar, K. S.; Tahir, M. N., A novel iodo bridged 1D Cu^{I} coordination polymer containing N,N-bidentate Schiff base ligand: Synthesis, structure, theoretical studies, electrochemical properties, and catalytic activity in the synthesis of tetrahydropyrimidines. *Polyheron* **2024**, *249*, 116754, DOI: 10.1016/j.poly.2023.116754.

[25] Kargar, K.; Centore, R.; Fallah-Mehrjardi, M.; Santagata, E.; Parisi, E.; Munawar, K. S., Synthesis and structural characterization of two novel cyano/isocyano bridged Cu^{I} coordination polymers: Catalytic activities in the synthesis of triazoles. *Inorg. Chim. Acta* **2025**, *581*, 122637, DOI: 10.1016/j.ica.2025.122637.

[26] X-RED32 (version 1.04), STOE & Cie, Darmstadt, Germany, **2002**.

[27] Sheldrick, G. M., SHELXT–Integrated space-group and crystal-structure determination. *Acta Crystallogr. A* **2015**, *71*, 3-8, DOI: 10.1107/S2053273314026370.

[28] Sheldrick, G. M., Crystal structure refinement with SHELXL. *Acta Crystallogr. C* **2015**, *71*, 3-8, DOI: 10.1107/S2053229614024218.

[29] Farrugia, L. J., WinGX and ORTEP for Windows: an update. *J. Appl. Crystallogr.* **2012**, *45*, 849-854, DOI: 10.1107/S0021889812029111.

[30] Macrae, C. F.; Edgington, P. R.; McCabe, P.; Pidcock, E.; Shields, G. P.; Taylor, R.; Towler, M.; Streek, J., Mercury: visualization and analysis of crystal structures. *Appl. Crystallogr.* **2006**, *39*, 453-457, DOI: 10.1107/S002188980600731X.

[31] Khandar, A. A.; Butcher, R. J.; Abedi, M.; Hosseini-Yazdi, S. A.; Akkurt, M.; Tahir, M. N., Synthesis, characterization and crystal structures of dinuclear macrocyclic Schiff base copper(I) complexes bearing different bridges. *Polyhedron* **2010**, *29*, 3178-3182, DOI: 10.1016/j.poly.2010.08.031.

[32] Ganguly, S.; Bauzá, A.; Frontera, A.; Ghosh, A., Tri-nuclear copper-cadmium complexes of a N_2O_2-donor ligand with the variation of counter anions: Structural elucidation and theoretical study on inter-molecular interactions. *Inorg. Chim. Acta* **2019**, *492*, 142-149, DOI: 10.1016/j.ica.2019.04.013.

[33] Mandal, S. K.; Thompson, L. K.; Newlands, M. J.; Gabe, E. J.; Nag, K., Structural and magnetic studies on macrocyclic dicopper(II) complexes. Influence of electron-withdrawing axial ligands on spin exchange. *Inorg. Chem.* **1990**, *29*, 1324-1327, DOI: 10.1021/ic00332a007.

[34] Spackman, P. R.; Turner, M. J.; McKinnon, J. J.; Wolff, S. K.; Grimwood, D. J.; Jayatilaka, D.; Spackman, M. A., CrystalExplorer: a program for Hirshfeld surface analysis, visualization and quantitative analysis of molecular crystals. *J. Appl. Crystallogr.* **2021**, *54*, 1006-1011, DOI: 10.1107/S1600576721002910.

[35] Spackman, M. A.; Jayatilaka, D., Hirshfeld surface analysis. *CrystEngComm* **2009**, *11*, 19-32, DOI: 10.1039/B818330A.

[36] Rubab, S. L.; Rehman, M. F. u.; Raza, A. R.; Ashfaq, M.; Al-Hussain, S. A.; Akhter, S.; Tahir, M. N.; Mustafvi, I.; Irfan, A.; Zaki, M. E. A., Synthesis, characterization, DFT calculations, comparative in vitro and in silico screening of anti-bacterial, anti-urease and α-amylase inhibition activities of indole derivatives with hirshfeld surface analysis and crystal structure explorations of Bis(4,6-dimethoxy-2,3-diphenyl-1H-7,7′-indolylmethane. *J. Mol. Struct.* **2025**, *1340*, 142476, DOI: 10.1016/j.molstruc.2025.142476.

[37] McKinnon, J. J.; Jayatilaka, D.; Spackman, M. A., Towards quantitative analysis of intermolecular interactions with Hirshfeld surfaces. *ChemComm*. **2007**, *53*, 3814-3816, DOI: 10.1039/B704980C.

[38] Kurbanova, M.; Ashfaq, M.; Ahsin, A.; Şahin, O.; Sayida, S.; Maharramov, A.; Tahir, M. N.; Abuelizz, H. A.; Al-Salahi, R.; El Bakri, Y., Crystalline salt synthesis from p-dimethylaminobenzaldehyde and o-phenylenediamine, single crystal XRD study along with computational investigation. *J. Mol. Struct.* **2025**, *1327*, 141156, DOI: 10.1016/j.molstruc.2024.141156.

[39] Turner, M. J.; McKinnon, J. J.; Jayatilaka, D.; Spackman, M. A., Visualisation and characterisation of voids in crystalline materials. *CrystEngComm* **2011**, *13*, 1804-1813, DOI: 10.1039/C0CE00683A.

[40] Frisch, M. J.; *et al.*, Gaussian 09, Revision B.01, Wallingford CT, **2009**.

[41] Becke, D., Density-functional thermochemistry. III. The role of exact exchange. *J. Chem. Phys.* **1993**, *98*, 5648-5652, DOI: 10.1063/1.464913.

[42] Weigend, F.; Ahlrichs, R., Balanced basis sets of split valence, triple zeta valence and quadruple zeta valence quality for H to Rn: design and assessment of accuracy. *Phys. Chem. Chem. Phys.* **2005**, *7*, 3297-3305, DOI: 10.1039/B508541A.

[43] Glendening, E. D.; Landis, C. R.; Weinhold, F., NBO 6.0: Natural bond orbital analysis program. *J. Comput. Chem.* **2013**, *34*, 1429-1437, DOI: 10.1002/jcc.23266.

[44] Daryanavard, M.; Jannesari, Z.; Javeri, M.; Abyar, F., A new mononuclear zinc(II) complex: Crystal structure, DNA- and BSA-binding, and molecular modeling; in vitro cytotoxicity of the Zn(II) complex and its nanocomplex. *Spectrochim. Acta - A: Mol. Biomol. Spectrosc.* 233 **2020**, 118175, DOI: 10.1016/j.saa.2020.118175.

[45] Dostani, M.; Kianfar, A. H.; Mahmood, W. A. K.; Dinari, M.; Farrokhpour, H.; Sabzalian, M. R.; Abyar, F.; Azarian, M. H., An experimental and theoretical study on the interaction of DNA and BSA with novel Ni^{2+}, Cu^{2+} and VO^{2+} complexes derived from vanillin bidentate Schiff base ligand. *Spectrochim. Acta - A: Mol. Biomol. Spectrosc.* **2017**, *180*, 144-153, DOI: 10.1016/j.saa.2017.02.047.

[46] Abyar, F.; Tabrizi, L., Experimental and theoretical investigations of novel oxidovanadium(IV) juglone complex: DNA/HSA interaction and cytotoxic activity. *J. Biomol. Struct. Dyn.* **2020**, *38*, 474-487, DOI: 10.1080/07391102.2019.1580221.

[47] Farrokhpour, H.; Hadadzadeh, H.; Darabi, F.; Abyar, F.; Rudbari, H. A.; Ahmadi-Bagheri, T., A rare dihydroxo copper(ii) complex with ciprofloxacin; a combined experimental and ONIOM computational study of the interaction of the complex with DNA and BSA. *RSC Adv.* **2014**, *4*, 35390-35404, DOI: 10.1039/C4RA04634J.

[48] Abyar, F.; Tabrizi, L., De Novo design of Cu(II) complex containing CNC-pincer-vitamin B3 and B7

conjugates for breast cancer application. *Mol. Pharm.* **2019**, *16*, 3802-3813, DOI: 10.1021/acs.molpharmaceut.9b00399.

[49] Mahadeva, P.; Revanasiddappa, H. D., Molecular docking analysis and spectroscopic investigations of cobalt(III), copper(II) and nickel(II) complexes of Schiff base ligand derived from metformin: evaluation of DNA binding, antioxidant and antimicrobial activities. *Biointerface Res. Appl. Chem.* **2024**, *14*, 19, DOI: 10.33263/BRIAC141.019.

[50] Trott O.; Olson, A. J., AutoDock Vina: improving the speed and accuracy of docking with a new scoring function, efficient optimization, and multithreading. *J. Comput. Chem.* **2010**, *31*, 455-461, DOI: 10.1002/jcc.2133.

[51] http://www.rcsb.org/structure

[52] Hetényi, C.; van der Spoel, D., Efficient docking of peptides to proteins without prior knowledge of the binding site. *Protein Sci.* **2002**, *11*, 1729-1737, DOI: 10.1110/ps.0202302.

[53] Hetényi, C.; van der Spoel, D., Blind docking of drug-sized compounds to proteins with up to a thousand residues. *FEBS Lett.* **2006**, *580*, 1447-1450, DOI: 10.1016/j.febslet.2006.01.074.

[54] Hetényi, C.; van der Spoel, D., Toward prediction of functional protein pockets using blind docking and pocket search algorithms. *Protein Sci.* **2011**, *20*, 880-893, DOI: 10.1002/pro.618.

[55] Adeleke, A. A.; Oladipo, S. D.; Zamisa, S. J.; Sanusi, I. A.; Omondi, B., DNA/BSA binding studies and *in vitro* anticancer and antibacterial studies of isoelectronic Cu(I)- and Ag(I)-pyridinyl-Schiff-base complexes incorporating triphenylphosphine as co-ligands. *Inorg. Chim. Acta* **2023**, *558*, 121760, DOI: 10.1016/j.ica.2023.121760.

[56] Sathiyaraj, S.; Sampath, K.; Butcher, R. J.; Pallepogu, R.; Jayabalakrishnan, C., Designing, structural elucidation, comparison of DNA binding, cleavage, radical scavenging activity and anticancer activity of copper(I) complex with 5-dimethyl-2-phenyl-4-[(pyridin-2-ylmethylene)-amino]-1,2-dihydro-pyrazol-3-one Schiff base ligand. *Eur. J. Med. Chem.* **2013**, *64*, 81-89, DOI: 10.1016/j.ejmech.2013.03.047.

[57] Zülfikaroğlu, A.; Çelikoğlu, E.; Çiğil. A. B., Synthesis and characterization of acrylate-functionalized Cu(II) hydrazone complexes: antimicrobial performance in UV-cured polyurethane coatings. *Mater. Today Commun.* **2025**, **49**, 113880, DOI: 10.1016/j.mtcomm.2025.113880.

[58] Moreira, J. M.; Vieira, S. d. S. F.; Correia, G. d. D.; de Almeida, L. N.; Finoto, S.; Brandl, C. A.; Msumange, A. A.; Galvão, F.; de Oliveira, K. M. P.; Paveglio, G. C.; da Silva, M. M.; Tirloni, B.; de Carvalho, C. T.; Roman, D., Synthesis and characterization of novel hydrazone complexes: exploring DNA/BSA binding and antimicrobial potential, *ACS Omega* **2025**, *10*, 7428-7440, DOI: 10.1021/acsomega.5c00069.